Role of the Dielectric Nature of the Transparent Contact in Charge Injection and Collection in Organic Optoelectronic Devices

Dor Gotleyb[1,*] and Rafi Shikler[1,2]

[1] *School of Electrical and Computer Engineering, Ben-Gurion University of the Negev, Beer-Sheva, Israel*
[2] *Ilse Katz Institute for Nanoscale Science and Technology, Ben-Gurion University of the Negev, Beer-Sheva, Israel*

(Received 3 January 2019; revised manuscript received 20 May 2019; published 16 July 2019)

We report for the first time on the implications of the dielectric nature of transparent electrodes, not only their low conductivity, but also on charge injection and collection. Transparent electrodes are common in organic-based optoelectronic devices because of the small diffusion length of charged carriers that requires complete coverage by the electrode. The commonly reported drawback of transparent electrodes is their low conductivity, which leads to unwanted power dissipation. However, there is no reference to the influence of the dielectric nature on the contact properties. The effect of the dielectric nature is introduced by modifying the expression for the image potential and the resulting barrier lowering at the transparent contact. The model is verified by fabricating and measuring simple unipolar devices, which show excellent agreement with the proposed modification. Without a modification, in order to have a good fitting, there should have been unrealistic values for some parameters, for example, a dielectric constant of 23 for the organic layer. The modified expression is then inspected in numerical simulations to study its nonlinear influence on the device. We find that using our model with typical device parameters, the predicted current density of the device is around half of the value calculated for a metallic electrode. Similar results are obtained by reducing the value of the mobility while keeping the injection condition for a metallic electrode. This explains why this property has been overlooked and is an indication of the extreme care needed when fitting experimental results.

DOI: 10.1103/PhysRevApplied.12.014029

I. INTRODUCTION

Organic optoelectronic devices are a promising technology with many unique applicative features. For example, Organic LEDs (OLEDs) are already being utilized in a variety of applications [1] with a market value of 25.5 $B in 2018 [2]. The ongoing progress in this field is accompanied by experimental as well as theoretical research aimed at extanding and enhancing the understanding of the physical processes in these devices [3–6]. A major part of this ongoing research is based on simulations whose role is to examine the physics and the behavior of the system as well as to extract essential parameters for research or for industrial purposes.

It is crucial to use accurate and physically justified models in order to have a reliable interpretation of the simulation results. In many cases, models have many parameters that make it difficult to distinguish between the functionalities of each parameter. Moreover, when some physical aspects are missing from the model and hence from the simulation, the measured results can still be fitted by tweaking other parameters for compensation. This might lead to incorrect extracted values of the parameters and might also be ill-matched with other measurements or other simulations [7]. As a result, there is a considerable number of inconsistencies in the literature regarding values of a variety of parameters characterizing a specific system under examination (devices, materials, etc.). For example, Blakesley *et al*. [8] constructed a single carrier device in order to extract its mobility. Afterward, the device was measured at two different laboratories and the results were then analyzed by three different scientists. Each time the value of the mobility was different, sometimes by more than one order of magnitude. Similarly, different systems or fabrication conditions can cause drastic changes in these parameters. This is presented in Ref. [9] where the importance of the conditions under which the electrode/organic interface is formed are discussed. The injection barrier (the difference between the electrode Fermi level and the HOMO or LUMO of the organic layer) can drastically vary and depends on a variety of conditions, such as the surface contamination and/or the degree of vacuum in the evaporation chamber, whether it is an organic on an electrode interface or an electrode on an organic interface, and so on. Thus, in many cases, correlating the experimental data to a certain model can lead to erroneous interpretation

*Gotleyb@post.bgu.ac.il

 © 2019 American Physical Society

of the physical processes. All these examples lead to the conclusion that the research cannot rely on experimental and fitting procedures alone. The justification of the physical basis for the model is crucial for getting a correct interpretation.

In this work, we focus attention on the role played by the contact materials in charge injection and collection. In organic optoelectronic devices, at least one electrode must be transparent to permit light to penetrate or leave the device (depending on the device type). One of the reasons is that a full electrode coverage reduces the charge carrier transport distance, which is primarily poor. This property cannot be achieved using conventional metallic electrodes, which are highly conductive and with approximately infinite permittivity at dc conditions since they are opaque. Conversely, materials such as Indium-Tin-Oxide (ITO) [10,11], Poly(3,4-ethylenedioxythiophene)-poly(styrenesulfonate) (PEDOT:PSS, which we will refer to as PP) [12–14] (used in ITO-free devices), and graphene [15,16] are widely used in the organic optoelectronic industry due to their high conductivity (although lower in comparison to metallic electrodes) and high transparency. The most familiar and prominent issue relating to their lower conductivity is power loss in the device [17–22].

However, an additional characteristic, which has been somewhat overlooked, is their dielectric property. Since these materials are either polymers or inorganic compounds, they are also dielectric materials [23]. They possess dielectric properties [24] and their static dielectric constant is finite [25]. In addition to these materials, there is a wide range of organic materials and inorganic dioxides that act as buffer layers between the electrode and the active layer. Their role is to improve the transport or injection of a specific charge carrier to the desired electrode or to block a charge carrier from getting to the electrode. Such materials can be the above-mentioned PP, Tris(8-hydroxyquinoline)aluminum(III) (Alq_3), lithium fluoride (LiF) [26], zinc oxide (ZnO) [27] (used in inverse organic photovoltaics), and so on. Wang *et al*. tested a couple of materials as Electron Injection Layers (EIL) and showed that their static dielectric constant has a strong impact on the OLED performance [28]. The static dielectric constants of the mentioned materials are presented in Table I. Although we will restrict the discussion in this paper to the electrode and active-layer interfaces, the concept presented in this work is also valid for these additional layers.

TABLE I. The static dielectric constants for different materials.

Materials	ε_r	Ref.	Materials	ε_r	Ref.
ITO	9.3	[29]	Alq_3	3	[30]
PP	3.9	[31]	LiF	∼9	[32]
Graphene	6.9	[33]	ZnO	∼8.5	[34]

Most models describing the contacts to organic devices were adopted from other fields and are sometimes inadequate for describing the functionality of dielectric electrodes. Among these models are the Ohmic contact model, which has no consideration of the electrode type at all, and the Schottky contact model [35]. Note that the latter model accounts for the effect of image potential [36], but only that which takes place near metals. The image potential effect is significant since it lowers the injection barrier at the electrode's interfaces and has a major impact on device performance.

A commonly used model for simulating organic devices is the one derived by Scott and Malliaras [37], which is suitable for both low and high applied voltages. In their model, the current flow is a contribution from charge injection (J_{inj}) and recombination (J_{rec}). Their model also accounts for the effect of the image charge. However, they considered only metallic electrodes. In this work, we examine the implications of replacing the metal electrode with a dielectric electrode. We reformulate the expression for the image potential effect in the Scott-Malliaras framework [37] to account for the properties of a dielectric electrode. This allows us to show the substantial difference between simulations based on metal and those based on dielectric electrodes. It must be pointed out that it is the static dielectric property that is important since the system is under quasistatic conditions.

The proposed model is tested by conducting experiments with two different device structures. To reduce the complexity and the number of device fitting parameters, we fabricate two different unipolar devices, one with a metal electrode and the other with a dielectric electrode. The first device structure is Au/organic-layer/Au, and the second is PP/organic-layer/Au.

In parallel, we demonstrate that a reduction in current density, which is predicted by the modification in the image potential, can also be obtained by reducing the mobility while keeping the metallic nature of the electrode. This emphasizes that excluding the effect of the dielectric electrode can cause significant inaccuracies in the predictions of the simulation fitting procedure. It is important to notice that the dielectric electrode effect is not limited to the drift-diffusion model with the Scott-Malliaras boundary conditions alone. The dielectric constant is presented in many other models, for example, in tunneling models (Fowler-Nordheim [38]) or hopping models (Arkhipov *et al*. [39]), which for some cases, can more accurately describe the system under consideration.

II. MODEL

In this section, we present the model of image potential and the difference in its implementation when a dielectric material (corresponding to the organic layer) has an interface with a metal or another dielectric material

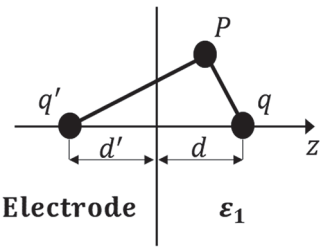

FIG. 1. A schematic representation of the electrode-dielectric interface. q, q' are the original and the image charges, respectively, and P is the test point.

(corresponding to the electrode). We revise the total potential energy near the electrodes, the expression for the barrier lowering which follows it, and the effect it has on the boundary conditions for the continuity equations.

The image potential (ϕ_{im}) is a result of the induced surface charge density due to the placement of a charge (q) in proximity to an electrode (at a distance d from the interface as shown in Fig. 1). The image potential modifies the overall potential acting on the original charge (q). The procedure for finding the image potential is based on the uniqueness theorem for the Poisson equation and is outlined in many textbooks [36]; in short, any solution satisfying the boundary conditions is feasible. We will briefly overview it here for the case of two dielectrics, a case not commonly dealt with in the literature.

At a dielectric-dielectric interface [40], the electric field is discontinuous and should satisfy the condition $\varepsilon_1 E_{1,n} = \varepsilon_2 E_{2,n}$. ε_1 and ε_2 are the static dielectric constants of the two materials, and the index n refers to the normal component of the electric field (E). Instead of solving the Poisson equation with the above boundary conditions, a pointlike charge q' can be placed at a distance d' from the interface inside the metal, where $d' = d$ (see Fig. 1). Replacing the initial surface charge with a properly chosen pointlike charge q', leads to the same induced image potential at the dielectric material (or organic layer) and hence is a solution to the same electrostatic problem.

To satisfy the mentioned boundary condition, the image charge takes on the following expression

$$q' = q^* q; \quad q^* = \frac{\varepsilon_1 - \varepsilon_2}{\varepsilon_1 + \varepsilon_2}. \tag{1}$$

q^* will be referred to as the Effective Interfacial Charge (EIC). This is similar to the effective mass that indicates a different charge carrier mass inside a material in comparison to free space. This result is a generalization of the metallic case in which the image charge must be equal to, and opposite in sign to the original charge ($q' = -q$); by setting ε_2 to approach infinity, the EIC goes back to $q^* = -1$.

As will be seen later, this difference has a major effect on the device performance. An interesting concept stemming from this result is that theoretically by setting a low dielectric electrode (or other buffer layer), the potential gets a positive sign, which, in turn, can repel charges from the contact [41–44]. Thus, it may be used as a charge blocking layer. Yet this idea is a matter for further investigation.

The induced image force acting on the original charge is now simply that of the pointlike image charge and takes the following form

$$F = q'q/[4\pi\varepsilon_0\varepsilon_1(d' + d)^2], \tag{2}$$

where ε_0 is the vacuum's permittivity. Substituting q', d' and integrating along the z axis gives the following image potential (ϕ_{img})

$$\phi_{\text{img}}(z) = -\frac{q^* q^2}{16\pi\varepsilon_0\varepsilon_1 z}. \tag{3}$$

The total potential energy (ϕ) near the interface can be expressed as a sum of three contributions, the barrier height (ϕ_B), the potential due to an external field (E), and the image potential, ϕ_{img}

$$\phi(z) = \phi_B - qEz - \frac{q^* q^2}{16\pi\varepsilon_0\varepsilon_1 z}. \tag{4}$$

This expression is a modification of the potential presented in Ref. [37]. The barrier lowering $\delta\phi$ (the difference between ϕ_B and the potential maximum, see Fig. 2) obtained from Eq. (4) is now given by $\delta\phi = \sqrt{q^* E/(4\pi q\varepsilon_0\varepsilon_1)}$. By redefining the Coulomb radius as $r_c = q^* q^2/(4\pi\varepsilon_0\varepsilon_1 K_B T)$, and using the reduced electric field $f = qEr_c/(K_B T)$, the barrier lowering can be written in its original form

$$\delta\phi = K_B T\sqrt{f}. \tag{5}$$

An illustration of the difference in Eqs. (4) and (5) due to the dielectric nature of the electrode is presented in Fig. 2. The barrier is shifted upward in the case of a dielectric electrode (indicated by *) in comparison to that of a metal electrode where $q^* = 1$.

Both ϕ_B and $\delta\phi$ are typically introduced in the models through a negative exponent that reduces the injected currents [35]. Thus, the modified value of the image charge has a major impact on the currents flowing in and out of the organic layer, especially at high applied voltages where $\delta\phi$ increases. In this work, we use the Scott-Malliaras current boundary condition approach. By repeating their derivation (see the work by Inganas *et al.* for derivation details [45,46]) and keeping in mind the EIC, we obtain the

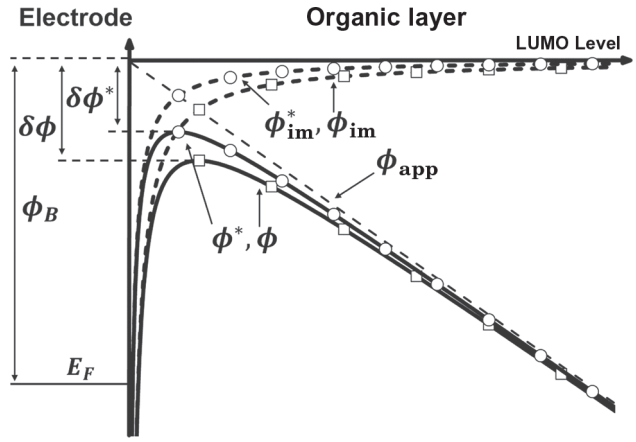

FIG. 2. Potential energy diagram at the electrode-organic-layer interface. The squared lines represent a device with a metal-like electrode ($q^* = 1$), whereas the circled lines and the symbols indicated by * represent a device with a dielectric electrode ($q^* \neq 1$). The short dashed lines are the image potentials ($\phi^*_{\rm im}$, $\phi_{\rm im}$), the dashed line is the external applied potential ($\phi_{\rm app}$), and the solid lines are the total potential energies (ϕ^*, ϕ). The junction barrier ϕ_B is lowered by an amount defined by either $\delta\phi^*$ or $\delta\phi$.

following expressions for the current boundary conditions

$$J_n^{\rm cat} = J_{\rm inj} - J_{\rm rec} = A_n^* T^2 \left[N_0 \exp\left(-\frac{\phi_{B,n}}{k_B T} + \sqrt{f} \right) - n \left(\frac{1}{\psi^2} - f \right) /4 \right], \tag{6}$$

$$J_p^{\rm an} = J_{\rm inj} - J_{\rm rec} = A_p^* T^2 \left[P_0 \exp\left(-\frac{\phi_{B,p}}{k_B T} + \sqrt{f} \right) - p \left(\frac{1}{\psi^2} - f \right) /4 \right]. \tag{7}$$

$J_n^{\rm cat}, J_p^{\rm an}$ are the electron and hole current densities at the cathode and anode, respectively. $A^*_{n(p)} = 16\pi\varepsilon_0\varepsilon_1\mu_{n(p)}K_B^2/(q^* q^2)$ is an effective Richardson constant, $\mu_{n(p)}$ and $N_0(P_0)$ are the electron (hole) mobility and the density of states for electrons (holes), respectively, $n(p)$ is the electron (hole) charge density, which must be determined self-consistently, and $\psi = f^{-1} + f^{-1/2} - f^{-1}\sqrt{1 + 2\sqrt{f}}$. The EIC parameter is presented only implicitly in Eqs. (6) and (7) in $A^*_{n(p)}, f$, and ψ. Thus, it is not straightforward to determine the influence of the EIC on the performance of the device. To do so, we conduct a series of device simulations and experiments to examine the implication of substituting a metal electrode with a conductive dielectric material.

III. METHODOLOGY

A. Experiment

The model is tested on two real devices that differ by their anode types, metallic (Au) and dielectric (PP) anodes. We choose to work with unipolar devices that are rather simple on one hand, but can also catch the essence of the dielectric-dielectric interface on the other hand. We choose two high work-function electrodes to ensure that the electron junction barriers will be very high and thus achieve a hole only device. As will be seen later from the simulation results, the hole junction barriers must be small enough to perceive the effect of the EIC. The junction barriers between Au or PP and the organic material N,N′-Bis(naphthalen-1-yl)-N,N′-bis(phenyl)benzidine (NPB), are approximately $\phi_B = 0.3$ eV [47–49].

The two devices are shown in Fig. 3. The devices are fabricated on top of a glass substrate that is precleaned in an ultrasonic bath with acetone, methanol, and isopropanol for 15 min each, after which they are placed in a plasma cleaning system for 4 min. On the first device, PP is spin-coated to act as the anode. To improve the anode's conductivity, we immerse the sample in methanol and follow the annealing sequence given in Ref. [50]. To avoid shunts between the PP layer and the top Au electrodes, the edges of the PP are removed. On the second device, we evaporate 5 nm of chrome (for adhesion) and 45 nm of Au through a shadow mask (again to prevent shorting with the top Au electrodes). Afterward, 100 nm of NPB is evaporated through a shadow mask leaving the middle of the device coated and the bottom electrode exposed. Then, a 50-nm top electrode of Au is evaporated. All evaporations are performed under an UHV of approximately 10^{-7} Torr. The cross section of the device (the overlapping between the anode and cathode) is measured to be $A = 2.38$ mm^2. All *I-V* measurements are carried out inside a glove box under a nitrogen environment to prevent degradation caused by oxidation and humidity [51].

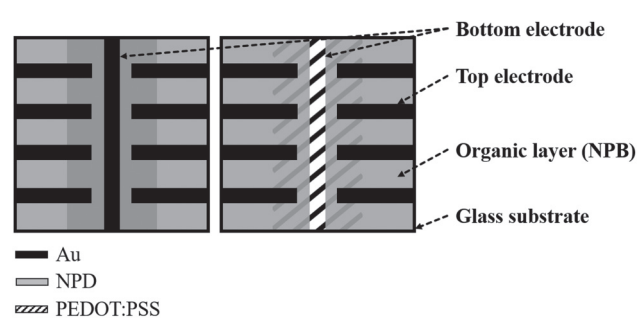

FIG. 3. A schematic illustration of the unipolar organic devices: (left) Au/NPB/Au, (right) PP/NPB/Au.

B. Simulations

Following the measurements, we conduct simulation of the device to check the validity of the modified model by comparing the predictions with the real devices. The simulation is based on the drift-diffusion model with three coupled differential equations, the Poisson equation, and electron−hole continuity equations. The Langevin recombination is considered. We also introduce the electric field mobility dependency, which needs to be considered in organic materials [52]. The dielectric constant and the hole mobility of NPB are chosen to be $\varepsilon_1 = 3, \mu_p^{\mathrm{NPB}} = 10^{-5}$ cm^2/V s [53], respectively.

The factor q^* is reflected in the boundary condition for the anode, as described by Eq. (7). The dielectric constant of the PP is $\varepsilon_2 = 3.9$, which makes the EIC very small, $q^* = 0.13$. This implies that PP is not ideal for anodes (or other buffer layers)with respect to the dielectric properties. For the device with Au, we use $q^* = 1$. The opposite boundary is described by Eq. (6). However, since the cathode is made from Au, it does not require any modification, ($q^* = 1$).

IV. RESULTS

A. Experiment

In this section, we present the experimental data as well as the simulation results of introducing the missing factor (q^*) in the boundary conditions for the continuity equations. The measured data and the simulation results are shown in Fig. 4. The squares and full line represent the measured data and numerical results for the device with a Au electrode and the circles and dashed line represent the measured data and numerical results for the device with a PP electrode. It is clearly seen that a very high precision fitting is achieved for both devices. The EIC modification in the model is needed for tracing the specific exponential shape revealed in the measurements of the device with the dielectric anode. Notably, an almost identical precision is obtained without the modification ($q^* = 1$). However, for that purpose, the dielectric constant of the organic layer is set to an unrealistic value, $\varepsilon_1 = 23$ (not shown in Fig. 4 since it overlaps the dashed line); a slightly lower precision is also obtained, but again, with an unrealistic low mobility ($\mu_p^{\mathrm{NPB}} = 10^{-7}$ cm^2/V s).

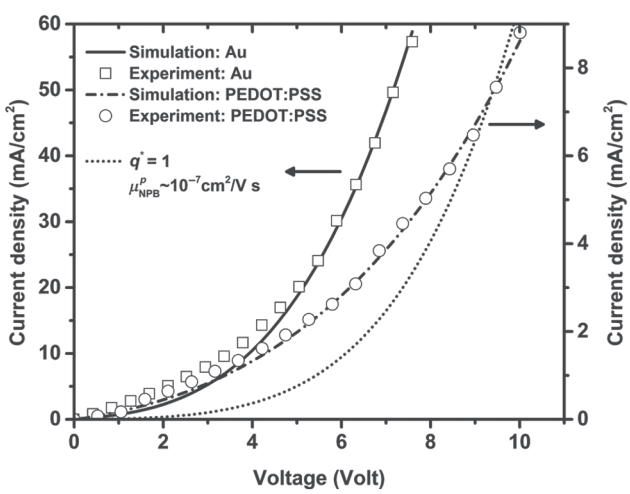

FIG. 4. *J-V* curves of the devices and respective numerical simulation results. (squares, full line) Au/NPB/Au and (circles, dashed line, dotted line) PP/NPB/Au.

B. Simulations

In order to emphasize the role of the boundary conditions and the EIC in particular, we conduct a series of simplified numerical simulations. The methodology of this analysis is to keep everything fixed apart from the boundary conditions for the hole injection at the anode [Eq. (7)]. This enables us to specifically trace the effect of the missing EIC in the expression for the anode boundary condition. We choose to work with arbitrary yet conventional values for the organic layer and with constant symmetric mobilities [54–56]. These values are summarized in Table II.

The anode is chosen to be the commonly used ITO with a relative permittivity of $\varepsilon_2 = 9.3$ [29]. This results in an image charge (q') that is approximately half the value ($q^* = 0.51$) of that of a metal electrode. The *J-V* curves for metal and dielectric electrodes are shown in Fig. 5.

The results reveal an extensive disparity between devices with metal compared to ITO anodes. This disparity might explain the over (or under) estimated values sometimes attained in simulations. As seen from the log scaled plot and the percentage difference presented in the inset, at low voltages, the two curves are considerably distinct. At 3 V it already reaches the 20% difference, and it increases to more than 30% at 6 V. In the high voltage region, the current density is significantly divergent and is exceeding 50% at above 10 V. Furthermore, with graphene or PP anodes, one can expect an even greater disparity due to their lower dielectric constants and lower EIC, $q^*_{\mathrm{graphene/PP}} = 0.39/0.13$. Nevertheless, there is

TABLE II. Parameters of the organic layer used in the simulations.

Parameter	Symbol	Value
Thickness (nm)	L	120
Dielectric constant (F/cm)	ε_1	3
Electron (Hole) mobility (cm^2/V s)	$\mu_{n(p)}$	10^{-4}
Effective density of states (cm^{-3})	$N_0(P_0)$	10^{20}
Anode, cathode work functions (eV)	$W_{\mathrm{an}}, W_{\mathrm{cat}}$	5.3, 4.2
Barrier for electrons at the cathode, Barrier for holes at the anode (eV)	$\phi_{B,n}^{\mathrm{cat}}, \phi_{B,p}^{\mathrm{an}}$	0.3

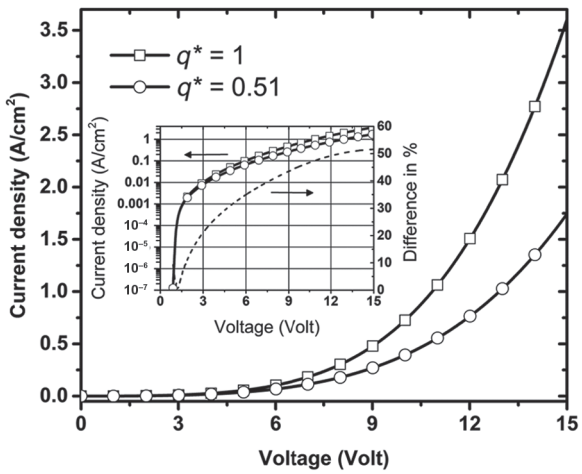

FIG. 5. *J-V* curves of devices with metal-like ($q^* = 1$) (squares), and with ITO ($q^* = 0.51$) (circles) anodes. The inset shows the log scale of the *J-V* curves and the difference in percentage between the two devices (deshed line).

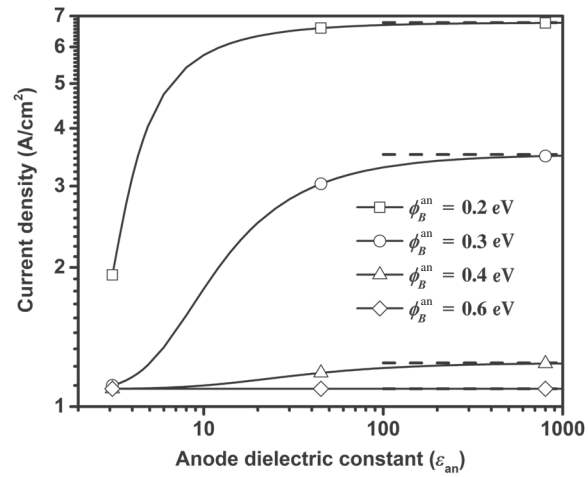

FIG. 7. Simulated current density in log scale as a function of the anode dielectric constant (starting from $\varepsilon_2 = 3.1$) for different hole injection barriers at the anode. The values of the current densities are taken at 15 V. The dashed lines are the current density values simulated with $q^* = 1$.

no clear relation between the value of the EIC and the ratio between the two curves.

Very similar results are also obtained by keeping $q^* = 1$, but using higher electron and hole mobilities. In Fig. 6, we have modified the mobilities to be $\mu_n = \mu_p = 5 \times 10^{-4}$ cm^2/V s. It can be seen that by ignoring the EIC, the mobilities are altered by a factor of 5 in order to get the same results as with q^*.

In Fig. 7, the current density of devices with different injection barriers (for holes at the anode side, and at 15 V) versus the dielectric constant of the anode is presented. The injection barrier for electrons at the cathode is kept at

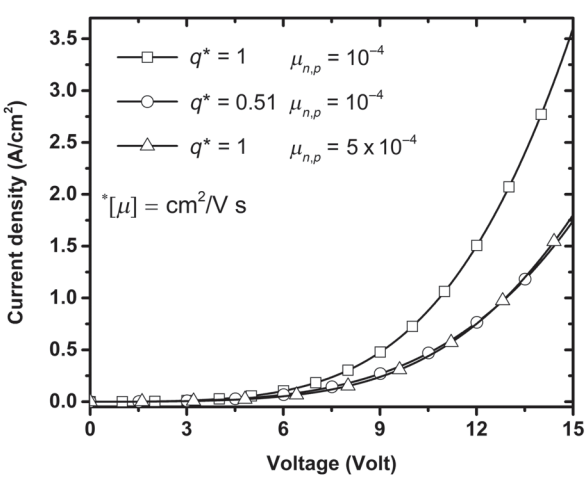

FIG. 6. Simulated *J-V* curves of three different devices. Square-line: $q^* = 1, \mu_n = \mu_p = 10^{-4}$, circle-line: $q^* = 0.51$, $\mu_n = \mu_p = 10^{-4}$, and triangle-line: $q^* = 1, \mu_n = \mu_p = 5 \times 10^{-4}$, ($[\mu] = \text{cm}^2/\text{V s}$).

$\phi_B^{\text{cat}} = 0.3$ eV. The dashed lines represent the current density without the modification. It can be seen that the current density approaches the condition of a metallike electrode as the dielectric constant of the anode increases. In addition, at $\varepsilon_2 = 3$, the effect of the image charge is canceled, thus only the initial injection barrier is relevant. At low dielectric constants, the current density is highly sensitive to this parameter. As the injection barrier decreases, the injection current increases and becomes even more sensitive to variations of the dielectric constant. Below $\phi_B^{\text{an}} = 0.4$ eV (triangle line), the barrier for holes becomes very insignificant compared to the lower $\phi_B^{\text{cat}} = 0.3$ eV. Thus, the effect of the anode becomes negligible and the current density is almost constant (see the diamond line in Fig. 7).

A clearer picture of the implication of modeling the anode as a dielectric material and its effect on the boundary conditions is reflected in Fig. 8. It shows the electron and hole current densities at the anode and cathode as a function of the applied voltage for a device with an ITO anode. The modification of only one boundary [Fig. 8(c)] affects every aspect of the device. The lower current injection at the dielectric-dielectric interface indicates a lower hole density profile, which, in response, reduces the recombination rate, and thus affects the densities' profiles throughout the device. This is a direct indication of the sensitivity of the model to the underlying physics.

As seen in the diamond line in Fig. 7, there are cases in which the hole current density at the anode is negligible. This case is demonstrated in Fig. 9 where we set the hole junction barrier at the anode to be $\phi_{B,p}^{\text{an}} = 0.6$ eV, hence effectively reducing the injection of holes into the organic layer.

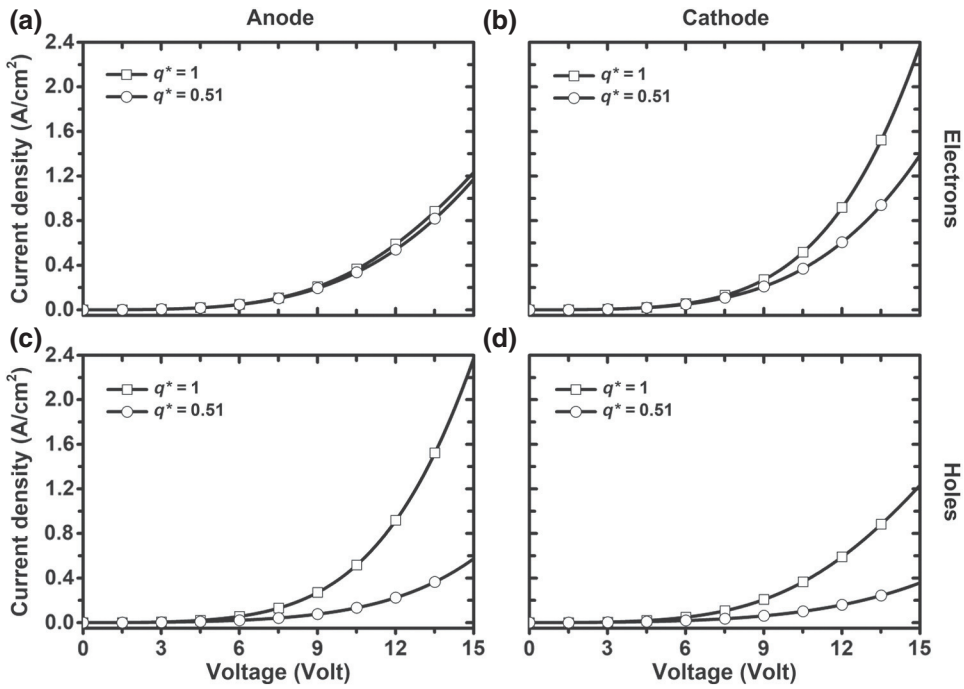

FIG. 8. Simulated (a, b) electron and (c, d) hole current densities at the organic-layer boundaries as a function of the applied voltage. The left- and righthand sides denote the (a, c) anode and the (b, d) cathode boundaries, respectively. The device with a metal-like anode ($q^* = 1$) represented by squares and that with an ITO ($q^* = 0.51$) represented by circles.

The value of the electron current density at the cathode [Fig. 9(b)] is orders of magnitude higher than the hole current density at the anode [Fig. 9(a)]. Therefore, the device performance is dictated only by the cathode boundary condition and the EIC modification has a negligible effect. However, devices such as OLEDs are two-charged carrier devices in which electrons and holes have approximately equal contributions. Thus, the effect of the dielectric anode is expected to be noticeable.

To conclude, the dielectric property of the transparent electrode is not considered in the commonly used models for charge injection and collection into organic-based optoelectronic devices. This property leads to a reduction of the image potential by a factor that depends on the dielectric constant of the electrode. This, in turn, diminishes the effect of the barrier lowering, which causes a reduction in the total current density. With our modification of the image potential, we could better fit the *I-V* curve of devices with a dielectric anode (a unipolar device with PP as the anode). Trying to fit the experimental data without this modification leads to nonrealistic values of parameters such as the organic dielectric constant of 23 or ultra-low mobility of 10^{-7} cm^2/V · sec. The effect of the EIC is further investigated using a self-consistent simulation to determine its nonlinear influence on device performance. We show that for typical device parameters, the current density of a device with $q^* = 0.51$ is reduced by over a half at high voltages. We also show that we can obtain the same results by using lower values for the mobilities while keeping the metallic boundary conditions, which can lead to incorrect predictions. In contrast, including the EIC effect in modeling the boundary conditions leads to more realistic simulations and to better and more accurate fittings.

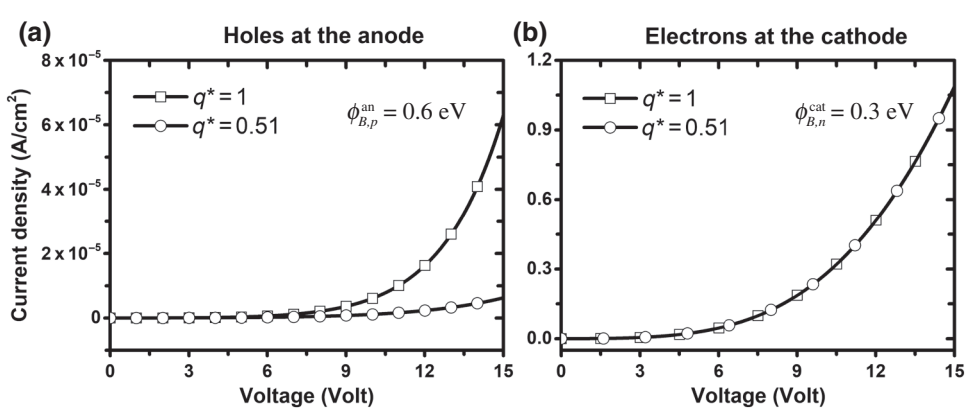

FIG. 9. (a) Hole current density at the anode and (b) electron current density at the cathode as a function of the applied voltage. The junction barriers for holes and electrons are $\phi_{B,p}^{an} = 0.6$ eV, $\phi_{B,n}^{cat} = 0.3$ eV, respectively. The device with a metal-like anode ($q^* = 1$) represented by squares and that with an ITO ($q^* = 0.51$) represented by circles.

ACKNOWLEDGMENT

This research was supported by THE ISRAEL SCIENCE FOUNDATION as part of the ISF-NSFC joint program. 2192/15

[1] C. Oh, H. Shin, W. Nam, B. Ahn, S. Cha, and S. Yeo, *21.1: Invited Paper: Technological Progress and Commercialization of OLED TV* (Wiley Online Library, 2013).

[2] Das Raghu, Ghaffarzadeh Khasha, and He Xiaoxi, OLED Display Market Sales to Hit $25.5 Bn in 2018, optics.org, 2018.

[3] M. Hilczer and M. Tachiya, Unified theory of geminate and bulk electron− hole recombination in organic solar cells, J. Phys. Chem. C **114**, 6808 (2010).

[4] M. Kuik, H. T. Nicolai, M. Lenes, G. A. Wetzelaer, M. Lu, and P. W. Blom, Determination of the trap-assisted recombination strength in polymer light emitting diodes, Appl. Phys. Lett. **98**, 45 (2011).

[5] S. R. Cowan, N. Banerji, W. L. Leong, and A. J. Heeger, Charge formation, recombination, and sweep-out dynamics in organic solar cells, Adv. Funct. Mater. **22**, 1116 (2012).

[6] C. Moon, K. Suzuki, K. Shizu, C. Adachi, H. Kaji, and J. Kim, Combined inter- and intramolecular charge-transfer processes for highly efficient fluorescent organic light-emitting diodes with reduced triplet exciton quenching, Adv. Mater. **29**, 1606448 (2017).

[7] N. Vukmirović and L. Wang, Carrier hopping in disordered semiconducting polymers: How accurate is the Miller–Abrahams model?, Appl. Phys. Lett. **97**, 160 (2010).

[8] J. C. Blakesley, F. A. Castro, W. Kylberg, G. F. Dibb, C. Arantes, R. Valaski, M. Cremona, J. S. Kim, and J. Kim, Towards reliable charge-mobility benchmark measurements for organic semiconductors, Org. Electron. **15**, 1263 (2014).

[9] J. Hwang, A. Wan, and A. Kahn, Energetics of metal–organic interfaces: New experiments and assessment of the field, Mater. Sci. Eng.: R: Rep. **64**, 1 (2009).

[10] B. G. Lewis and D. C. Paine, Applications and processing of transparent conducting oxides, MRS Bull. **25**, 22 (2000).

[11] T. Minami, Present status of transparent conducting oxide thin-film development for Indium-Tin-Oxide (ITO) substitutes, Thin Solid Films **516**, 5822 (2008).

[12] Y. Galagan, J. J. Rubingh, R. Andriessen, C. Fan, P. W. Blom, S. C. Veenstra, and J. M. Kroon, ITO-free flexible organic solar cells with printed current collecting grids, Solar Energy Mater. Solar Cells **95**, 1339 (2011).

[13] Y. Galagan, E. W. Coenen, S. Sabik, H. H. Gorter, M. Barink, S. C. Veenstra, J. M. Kroon, R. Andriessen, and P. W. Blom, Evaluation of ink-jet printed current collecting grids and busbars for ITO-free organic solar cells, Solar Energy Mater. Solar Cells **104**, 32 (2012).

[14] D. Angmo, I. Gonzalez-Valls, S. Veenstra, W. Verhees, S. Sapkota, S. Schiefer, B. Zimmermann, Y. Galagan, J. Sweelssen, and M. Lira-Cantu, Low-cost upscaling compatibility of five different ITO-free architectures for polymer solar cells, J. Appl. Polym. Sci. **130**, 944 (2013).

[15] X. Wang, L. Zhi, and K. Müllen, Transparent, conductive graphene electrodes for dye-sensitized solar cells, Nano Lett. **8**, 323 (2008).

[16] J. Yoon, H. Sung, G. Lee, W. Cho, N. Ahn, H. S. Jung, and M. Choi, Superflexible, high-efficiency perovskite solar cells utilizing graphene electrodes: towards future foldable power sources, Energy Environ. Sci. **10**, 337 (2017).

[17] S. Yoo, B. Domercq, and B. Kippelen, Intensity-dependent equivalent circuit parameters of organic solar cells based on pentacene and C 60, J. Appl. Phys. **97**, 103706 (2005).

[18] D. Gupta, M. Bag, and K. S. Narayan, Area dependent efficiency of organic solar cells, Appl. Phys. Lett. **93**, 384 (2008).

[19] S. Choi, W. J. Potscavage Jr, and B. Kippelen, Area-scaling of organic solar cells, J. Appl. Phys. **106**, 054507 (2009).

[20] J. D. Servaites, S. Yeganeh, T. J. Marks, and M. A. Ratner, Efficiency enhancement in organic photovoltaic cells: consequences of optimizing series resistance, Adv. Funct. Mater. **20**, 97 (2010).

[21] A. Manor, E. A. Katz, T. Tromholt, B. Hirsch, and F. C. Krebs, Origin of size effect on efficiency of organic photovoltaics, J. Appl. Phys. **109**, 074508 (2011).

[22] D. Gotleyb and R. Shikler, A new model of organic solar cells reveals open circuit conditions and size dependent power loss induced by the finite conductivity of a transparent contact, J. Appl. Phys. **121**, 045502 (2017).

[23] J. Ederth, P. Heszler, A. Hultåker, G. A. Niklasson, and C. G. Granqvist, Indium tin oxide films made from nanoparticles: models for the optical and electrical properties, Thin Solid Films **445**, 199 (2003).

[24] E. A. Alwan, A. Kiourti, and J. L. Volakis, Indium tin oxide film characterization at 0.1–20 GHz using coaxial probe method, IEEE Access **3**, 648 (2015).

[25] I. Hamberg and C. G. Granqvist, Evaporated Sn-doped In_2O_3 films: Basic optical properties and applications to energy-efficient windows, J. Appl. Phys. **60**, R123 (1986).

[26] F. J. Lim, K. Ananthanarayanan, J. Luther, and G. W. Ho, Influence of a novel fluorosurfactant modified PEDOT: PSS hole transport layer on the performance of inverted organic solar cells, J. Mater. Chem. **22**, 25057 (2012).

[27] Y. Sun, J. H. Seo, C. J. Takacs, J. Seifter, and A. J. Heeger, Inverted polymer solar cells integrated with a low-temperature-annealed sol-gel-derived ZnO film as an electron transport layer, Adv. Mater. **23**, 1679 (2011).

[28] F. Wang, S. Liu, and C. Zhang, The dielectric constant of materials effect the property of the OLED, Microelectron. J. **38**, 259 (2007).

[29] F. Yi, E. Shim, A. Y. Zhu, H. Zhu, J. C. Reed, and E. Cubukcu, Voltage tuning of plasmonic absorbers by indium tin oxide, Appl. Phys. Lett. **102**, 221102 (2013).

[30] R. L. Martin, J. D. Kress, I. H. Campbell, and D. L. Smith, Molecular and solid-state properties of tris-(8-hydroxyquinolate)-aluminum, Phys. Rev. B **61**, 15804 (2000).

[31] C. Uher, *Materials Aspect of Thermoelectricity* (CRC Press, 2016).

[32] K. F. Young and H. Frederikse, Compilation of the static dielectric constant of inorganic solids, J. Phys. Chem. Ref. Data **2**, 313 (1973).

[33] J. Fang, W. G. Vandenberghe, and M. V. Fischetti, Microscopic dielectric permittivities of graphene nanoribbons and graphene, Phys. Rev. B **94**, 045318 (2016).

[34] N. Ashkenov, B. N. Mbenkum, C. Bundesmann, V. Riede, M. Lorenz, D. Spemann, E. M. Kaidashev, A. Kasic, M. Schubert, and M. Grundmann, Infrared dielectric functions and phonon modes of high-quality ZnO films, J. Appl. Phys. **93**, 126 (2003).

[35] J. C. Scott, Metal–organic interface and charge injection in organic electronic devices, J. Vac. Sci. Technol. A: Vac. Surf. Films **21**, 521 (2003).

[36] D. J. Griffiths, *Introduction to Electrodynamics* (Prentice-Hall, NJ, 1999).

[37] J. C. Scott and G. G. Malliaras, Charge injection and recombination at the metal–organic interface, Chem. Phys. Lett. **299**, 115 (1999).

[38] M. Lenzlinger and E. H. Snow, Fowler-Nordheim tunneling into thermally grown SiO_2, J. Appl. Phys. **40**, 278 (1969).

[39] V. I. Arkhipov, E. V. Emelianova, Y. H. Tak, and H. Bässler, Charge injection into light-emitting diodes: Theory and experiment, J. Appl. Phys. **84**, 848 (1998).

[40] T. Sometani, Image method for a dielectric plate and a point charge, Eur. J. Phys. **21**, 549 (2000).

[41] C. Wagner, Die Oberflächenspannung verdünnter elektrolytlösungen, Phys. Z **25**, 474 (1924).

[42] L. Onsager and N. N. Samaras, The surface tension of Debye-Hückel electrolytes, J. Chem. Phys. **2**, 528 (1934).

[43] V. S. Markin and A. G. Volkov, Quantitative theory of surface tension and surface potential of aqueous solutions of electrolytes, J. Phys. Chem. B **106**, 11810 (2002).

[44] K. A. Karraker and C. J. Radke, Disjoining pressures, zeta potentials and surface tensions of aqueous non-ionic surfactant/electrolyte solutions: theory and comparison to experiment, Adv. Colloid Interface Sci. **96**, 231 (2002).

[45] S. Lacic and O. Inganäs, Modeling electrical transport in blend heterojunction organic solar cells, J. Appl. Phys. **97**, 124901 (2005).

[46] J. A. Barker, C. M. Ramsdale, and N. C. Greenham, Modeling the current-voltage characteristics of bilayer polymer photovoltaic devices, Phys. Rev. B **67**, 075205 (2003).

[47] S. O. Kasap, *Principles of Electronic Materials and Devices* (McGraw-Hill, New York, 2006).

[48] T. Chu and O. Song, Thickness dependence of the trap states in organic thin film of N, N′-bis (naphthalen-1-yl)-N, N′-bis (phenyl) benzidine, Appl. Phys. Lett. **91**, 073508 (2007).

[49] M. R. Lenze, N. M. Kronenberg, F. Würthner, and K. Meerholz, In-situ modification of PEDOT: PSS work function using alkyl alcohols as secondary processing solvents and their impact on merocyanine based bulk heterojunction solar cells, Org. Electron. **21**, 171 (2015).

[50] Y. H. Kim, C. Sachse, M. L. Machala, C. May, L. Müller-Meskamp, and K. Leo, Highly conductive PEDOT: PSS electrode with optimized solvent and thermal post-treatment for ITO-free organic solar cells, Adv. Funct. Mater. **21**, 1076 (2011).

[51] S. Nabha-Barnea, N. Maman, I. Visoly-Fisher, and R. Shikler, Microscopic investigation of degradation processes in a polyfluorene blend by near-field scanning optical microscopy, Macromolecules **49**, 6439 (2016).

[52] P. Blom, M. De Jong, and M. G. Van Munster, Electric-field and temperature dependence of the hole mobility in poly (p-phenylene vinylene), Phys. Rev. B **55**, R656 (1997).

[53] T. Chu and O. Song, Hole mobility of N, N′-bis (naphthalen-1-yl)-N, N′-bis (phenyl) benzidine investigated by using space-charge-limited currents, Appl. Phys. Lett. **90**, 203512 (2007).

[54] P. S. Davids, I. H. Campbell, and D. L. Smith, Device model for single carrier organic diodes, J. Appl. Phys. **82**, 6319 (1997).

[55] C. Blades and A. B. Walker, Simulation of organic light-emitting diodes, Synth. Met. **111**, 335 (2000).

[56] A. P. Kulkarni, C. J. Tonzola, A. Babel, and S. A. Jenekhe, Electron transport materials for organic light-emitting diodes, Chem. Mater. **16**, 4556 (2004).